Enhanced dielectric properties of PVA/PEDOT:PSS/MnO$_2$ based composites for electronic applications

J. Gokul Raja[1], M. Basheer Ahamed[1,*] (iD), Chaudhery Mustansar Hussain[2], and Paavai Era[3]

[1] Department of Physics, B. S. Abdur Rahman Crescent Institute of Science and Technology, Vandalur, Chennai 600048, India
[2] Department of Chemistry and Environmental Science, New Jersey Institute of Technology, Newark, NJ 07102, USA
[3] Department of Physical Sciences, Saveetha University, Chennai 602105, India

ABSTRACT

Polymer composite (PC) films comprising polyvinyl alcohol (PVA) and poly(3,4-ethylene dioxythiophene):poly(styrene sulfonate) (PEDOT:PSS) with manganese dioxide (MnO$_2$) as filler were prepared by simple solution casting method. The structural confirmation of PCs was investigated by Fourier transform Infrared Spectroscopy (FTIR) and X-ray diffraction (XRD) techniques. The morphological and thermal properties were analyzed using scanning electron microscope (SEM) and thermogravimetric analysis (TGA). Under the frequency range, 50 Hz to 20 MHz, and temperature from 40 to 150 °C, the dielectric properties and Q-factor values for the as-synthesized PC films were investigated by an impedance analyzer. PVA/PEDOT:PSS/MnO$_2$ having wt% 50:35:15 revealed high dielectric constant (ε) at 1949 and low dielectric loss(tanδ) at 8.13. The obtained results suggest that the titled PC films are effective materials for energy storage applications.

1 Introduction

The synthesis of Polymer composite films has been an emerging techno-support in materials fabrication research in recent decades. Due to its (PC films) commendable weight, and physical, chemical, optical, and thermal properties, it has been the unique and finest solution for a wide range of applications in fabricating electronic and electrical devices. Conducting polymers is essential to have huge potential in capacitors and electronic device applications. Among these, the polymer blend provides unique physical, thermal and chemical properties and the dispersion of filler particles in the polymer blend enhances these properties. The homogeneous dispersion must cause percolation, wherein the filler particles form a chain in the polymer blend to have a good conductivity at a particular temperature [1]. Based on the type of the polymer and the size and concentration of the filler particles dispersed into the matrix, the characterization of the PC film is determined.PC films having high dielectric constant, surface area, and excellent thermal stability can store high electrical energy and possess good conductivity.

Address correspondence to E-mail: basheerahamed@crescent.education

Springer

In literature, other than polymers metallic substrates were also been widely used to synthesize composite films through various methods such as electrochemical deposition of bismuth (Bi) for EMI shielding [2] and high current density [3] applications. Some other significant techniques are Corrosive resistive Ni/Al nanocomposites by electrochemical method [4], synthesis of hard/soft ferrites through one-pot citrate combustion technique [5] and binary/ternary composite through mechanical mixing followed by thermal pressing [6] for biomedical, permanent magnets and high-frequency functional applications respectively.

PVA is a cost-effective, water-soluble and non-conductive soft polymer having a melting point of 230 °C and for the fully and partially hydrolyzed PVA grades the melting point is between 180 and 190 °C [7]. It has a wide range of properties such as biocompatibility, biodegradability, stability in chemical and thermal conditions with various molecular weight%, non-carcinogenicity, processability, good elasticity, chemically resistant, and fair emulsifier [8–12], etc. It also has excellent physical, chemical, adhesive, and mechanical properties [12, 13]. Due to its synthetic nature, non-toxicity, and semi-crystalline, PVA exhibits high dielectric strength (> 1000 kV/mm) [14], excellent transparency, good film-forming capability, hydrophilicity, and high density in chemically reactive functionalities and also is used as a cross-linker [15, 16]. It enhances durability and gives a correct fracture strain and good tensile strength for the synthesized PC films [17]. Though there are several properties of PVA, pure PVA acts as a poor conductor due to hydrogen bonding interactions between the hydroxyl groups of PVA molecules and complex molecular formation. Also, as the polymer chain in PVA is closely packed due to the inter and intramolecular H-bonding interactions, its less permeation flux results in a PVA membrane [18]. PVA has many applications in optical sensors, photovoltaic cells, image storage, and biomedical devices [19]. PVA works as an excellent host polymer in forming blended polymers, and the low conductivity of pure PVA can be increased by blending it with other conducting polymers[20].

Conducting polymers possess good electric conductivity, increased charge–discharge rates, greater surface area, excellent potential in redox reactions, and good transportation of ions and electrons when used as electrodes in energy storage systems [21, 22].

Intrinsic conducting polymers (ICP) are free from doping and are electroneutral [23]. PEDOT:PSS is one of the promising polymers discussed in the present work that acquires intrinsic electrical conductivity. The double bond conjugated polymer arrangement in it makes less elastic [24, 25]. The oligomeric PEDOT is bonded with the PSS chain by electrostatic forces [26] forming PEDOT positive charges and PSS negative charges. Being polyelectrolyte, PSS makes PEDOT soluble in water [27]. PEDOT:PSS is a biocompatible, conducting, and versatile electroactive polymer. It also has solution processability, transparency, and mechanical properties such as flexibility. The dispersion of PEDOT:PSS is good in water and polar organic solvents and it has high transparency in the visible range spectrum. Also, due to electrochemical stability, and high conductivity, the organic conducting polymer PEDOT:PSS is used as an electrode in supercapacitors for storing charges [28], solar cells, actuators and sensors [29]. The electrical conductivity of the ICP can be improved by secondary doping and stretchability can be enhanced by blending the PEDOT:PSS with a soft polymer [30]. This alters the chemical structure of the molecule, giving better tunable, redox, and electronic functions [23]. Polymer blend prepared forms better wettability than pure PEDOT:PSS when the solution is in glass substrates, which denotes the better film-forming capability of the as-synthesized polymer blend solution [31]. The conductivity increases from 0.2 to 75 S/cm for PVA/PEDOT:PSS blend [25]. PVA forms good intermolecular hydrogen bonding with PEDOT:PSS because it has hydroxyl groups that are linked with methane carbons [20]. As the wt% of the active material PEDOT:PSS is increased, energy density and specific capacitance are also increased [32]. This makes the PVA/PEDOT:PSS film to be flexible, processable, and conductive.

Due to the multivalent states, the metallic transition elements Mn, Co, and Ru are focussed greatly by the researchers to develop them as electroactive materials [33]. To enhance the efficiency of the electrodes in supercapacitors, transition metal oxides such as RuO_2 and MnO_2 are used instead of carbon materials [22]. MnO_2 is found abundant on earth, has lower toxicity, is cost-effective, and eco-friendly. All these increase its significance in the research field since 1990s [34]. It also possesses better electrochemical performances, a large voltage range, heterogeneous catalytic activity, and good

reversibility in redox reactions [22, 23, 27, 33]. Having good chemical and physical properties [35], MnO_2 acts as the most hotspot material providing high specific capacitance, better cyclic stability, and high surface area [36, 37]. Due to their energy density and high power density, it is used as electrodes in energy storage devices [38]. Mn is the best transition metal for the transportation of electrons in capacitors [39]. Though MnO_2 has lower conductivity ($\sim 10^{-6}$ S/m) [40] and breakability, it is morphologically dense [41]. Mn is used as a dopant to decrease the wide bandgap energy of PEDOT:PSS. So by minimizing the optical band gap, due to interatomic transitions the electric conductivity and energy storage capacity of the as-synthesized PC film is increased [34]. The spongy structure of PEDOT:PSS has an efficient conducting network. MnO_2 being a good capacitive material dispersive in PEDOT:PSS increases the energy storage efficiency [42].

In the current work, PVA/PEDOT:PSS/MnO_2 films were fabricated by conventional and cost-effective solution mixing and casting method. PVA and PEDOT:PSS solutions are prepared, blended, and dispersed with MnO_2 fillers. The as-synthesized novel PVA/PEDOT:PSS/MnO_2 composite film gives a high dielectric constant and low dielectric loss which serves as an effective and essential charge storage device. As per the literature survey, for the first time, efforts have been put forward to enhance the dielectric and thermal stability by increasing the MnO_2 filler content in PVA/PEDOT:PSS blend. The thermal behaviour of composites reveals the fire retardant properties and makes the film best suited for electronic devices. This manuscript reports the preparation of PC films under different compositions and investigates the structural, morphological, thermal, and dielectric properties through appropriate characterization techniques.

2 Experimental

2.1 Materials

PVA of molecular weight of 115,000 g/mol and hydrolysis 98–99 mol% was procured from Loba Chemi Pvt.Ltd, Mumbai, India. Poly(3,4ethylene-dioxythiophene):poly(styrene sulfonate (PEDOT:PSS) having high conductive grade (> 200 S/cm) with a density of 1.011 g/cm^3 was purchased from Sigma

Aldrich, Germany. Manganese dioxide (MnO_2) powder in the micron range having a molecular weight of 86.94 g/mol and melting point of 535 °C was acquired from Sisco Research Laboratories Pvt. Ltd, Mumbai, India.

2.2 Synthesis of PVA/PEDOT:PSS/MnO_2 composite films

Figure 1 demonstrates the synthesis procedure of PVA/PEDOT:PSS/MnO_2 composite films. 0.5 g of PVA powder was dissolved in 20 ml of distilled water by heating the PVA solution at 90 °C for 2 h followed by stirring for 1 h. 0.45 g of PEDOT:PSS was dissolved in 10 ml of distilled water and stirred for 3 h and then the solution was slowly added to the PVA solution in drops under a continuous stirring process. 0.05 g of MnO_2 powder was dispersed in 10 ml distilled water by continuous stirring for 8 h followed by sonication over 2 h. The MnO_2 solution was then homogeneously dispersed in the PVA/PEDOT:PSS blend solution by sonicating the whole solution for 2 h followed by vigorous stirring for 8 h at 650 rpm at room temperature (RT). The solution obtained was cast in a Teflon Petri dish and dried in the hot air oven at 60 °C for 5 h for the solvent to evaporate completely. The prepared PVA/PEDOT:PSS composite film of thickness 60–80 μm shown in Fig. 1 was carefully peeled from the Petri dish and utilized for further characterization. The procedure was repeated for different feed compositions of PVA, PEDOT:PSS and MnO_2 filler as shown in Table 1.

2.3 Characterizations

FTIR spectroscopy of as-synthesized PVA/PEDOT:PSS/MnO_2 composites film was carried out with Fourier Transform Infrared Spectrophotometer (Shimadzu, IRAffinity-1, Japan) in the wavenumber range 400–4000 cm^{-1}. The spectra were taken in transmittance mode.

X-ray diffraction (XRD) patterns of pure PVA, PVA/PEDOT:PSS blend, and PVA/PEDOT:PSS/MnO_2 composite films with various MnO_2 loadings were examined using the D8 Bruker advanced X-ray diffractometer, with Cu Kα radiation of wavelength (λ = 1.5406 Å). The XRD patterns were measured in the 2θ range from 10 to 80° with 1°/min scanning rate and 0.01° step size.
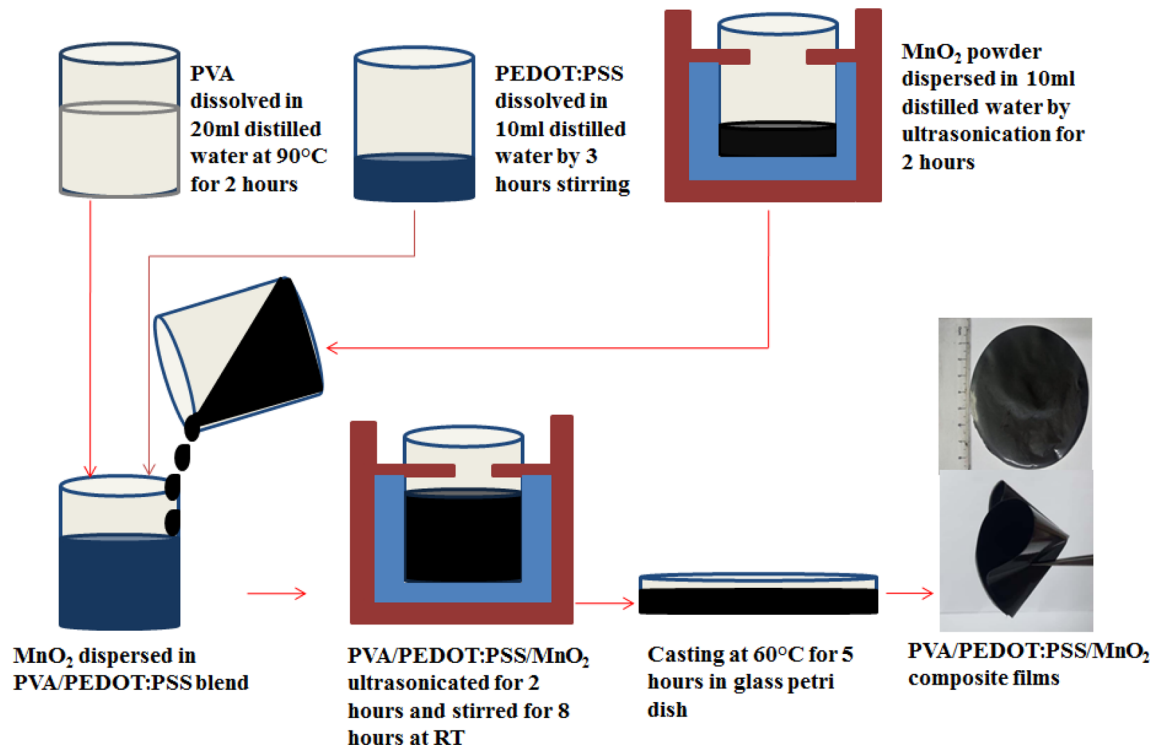
Fig. 1 Synthesis protocol of PVA/PEDOT:PSS/MnO$_2$ composite films

Table 1 Feed compositions of PVA/PEDOT:PSS/MnO$_2$ composite films

Sample	PVA (wt%)	PEDOT:PSS (wt%)	MnO$_2$ (wt%)
(a)	100	0	0
(b)	50	50	0
(c)	50	45	5
(d)	50	35	15
(e)	50	25	25
(f)	50	20	30

The surface morphology of PVA/PEDOT:PSS/MnO$_2$ composites was analyzed using ZEISS Scanning Electron Microscope with energy-dispersive X-ray spectroscopy (EDS), Germany with an applied accelerating voltage of 20 kV.

Thermal stability of PVA/PEDOT:PSS/MnO$_2$ composite films was evaluated by Shimadzu TGA 50 series thermogravimetric analyzer (TGA) operated under N$_2$ as a purge gas. Samples were heated up to 800 °C at a rate of 20 °C/min.

The electrical properties of PVA/PEDOT:PSS/MnO$_2$ composite films with various MnO$_2$ loadings were evaluated using a PSM1735 impedance analyser (Newtons 4th Ltd., UK). The measurements were carried out over a 40 °C to 150 °C temperature range with frequencies ranging from 50 Hz to 20 MHz.

3 Results and discussion

3.1 FTIR Characterization

The various functional groups present in the as-synthesized PVA/PEDOT:PSS/MnO$_2$ composite films were depicted by the FTIR spectra and is shown in Fig. 2. In the FTIR spectra of pure PVA, the broadband ranging from 3003 to 3684 cm^{-1} attributes to the O–H stretching vibrations of the hydroxyl groups present in PVA polymer [43]. The peak around 2928 cm^{-1} corresponds to the asymmetric C–H stretching vibrations [44]. The peak at 1714 cm^{-1} corresponds to C=O stretching vibrations of the group vinyl acetate and the peak at 1084.7 cm^{-1} is due to the C–O stretching of the acetyl group in the PVA polymer [45]. The peak at 1420 cm^{-1} ascribes to the CH$_2$ bending vibration of PVA aldehyde groups and the peak at 1330.6 cm^{-1} corresponds to CH$_2$ wagging vibrations [46]. The skeletal vibrations of PVA are observed at bands of 919.8 cm^{-1} and 836.9 cm^{-1} [44]. In the FTIR spectra of the PVA/
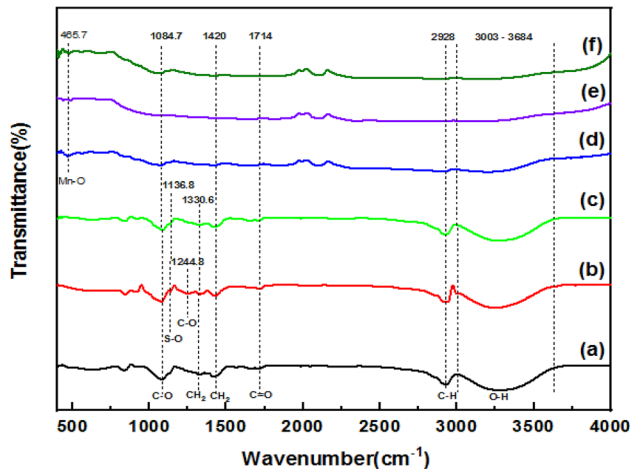
Fig. 2 FTIR spectra of **a** pure PVA, **b** PVA/PEDOT:PSS at 50:50 wt% and PVA/PEDOT:PSS/MnO₂ at **c** 50:45:05 wt%, **d** 50:35:15 wt%, **e** 50:25:25 wt%, **f** 50:20:30 wt%

PEDOT:PSS blend, the peak due to O–H stretching vibrations shifts from 3284 cm^{-1} of pure PVA to a low wavenumber of 3248.5 cm^{-1}. This occurs because of H-bonding interactions of hydroxyl groups between PEDOT:PSS and PVA [47]. Some new peaks arise at 1244.8 cm^{-1} which ascribes to the C–O stretching vibrations and the peak at 1136.8 cm^{-1} corresponding to S–O bonds [48]. In the PVA/PED-OT:PSS/MnO₂ composite films under different compositions from Fig. 2(c-f), the peaks broaden due to strong intermolecular interactions in the dispersion of MnO₂ fillers. This may be due to the effect of increased concentration of the MnO₂ fillers and a new peak arises at 465.7 cm^{-1} attributing to Mn–O stretching [49] which confirms the excellent dispersion of MnO₂ in the PVA/PEDOT:PSS blend.

3.2 XRD characterization

The investigation of structural properties and crystalline planes of the titular PVA/PEDOT:PSS/MnO₂ composite films was done through XRD analyses. The XRD diffraction pattern is plotted in the range of 2θ from 10 to 80°. In the plot, Fig. 3a denotes the diffraction pattern of pure PVA. The very broad peak at $2\theta = 19.5°$ corresponds to the orthorhombic lattice of the crystal phase (101) [48]. Pure PVA attributes to excellent intra and intermolecular H- bondings interactions between the PVA monomer units [50]. The imperfect crystalline lattice of PVA has PVA amorphous phase filling up the empty volume which contributes to the semi-crystalline phase (i.e. both

crystalline and amorphous phase) [12]. In Fig. 3b, PVA/PEDOT:PSS blend with 50:50 wt% proves the intermolecular hydrogen bonding interactions among the polymer molecular chains. In the PC films from Fig. 3c–f, the MnO₂ fillers are dispersed in the PVA/PEDOT:PSS blend at different concentrations. A peak with high intensity arises at 28.6° ascribing to the (310) crystal plane [51]. As there is an increase in the wt% of MnO₂ fillers and a decrease in PEDOT:PSS wt%, the intensity of the broad peak at 19.5° increases and small peaks arise at 37.3, 41, 51.1, 59.1 degrees corresponding to the crystal planes (211), (301), (411), (521) [37, 51, 52] with increasing intensity and crystallinity. The slight displacements in peaks are caused due to lattice distortions by varying concentrations [53]. The high intense peak at 28.6° shifts to a lower diffraction angle of 28.45° corresponding to lesser H-bonding interactions between MnO₂ and PVA/PEDOT:PSS blend. Thus, by the homogeneous dispersion of MnO₂ in the PVA/PEDOT:PSS blend, the crystallinity of the PC increases, and it may lead to a change in different structural properties.

3.2.1 Crystallite size and strain

The crystallite size of the as-synthesized PVA/PED-OT:PSS/MnO₂ film was calculated using the Debye Scherrer formula,

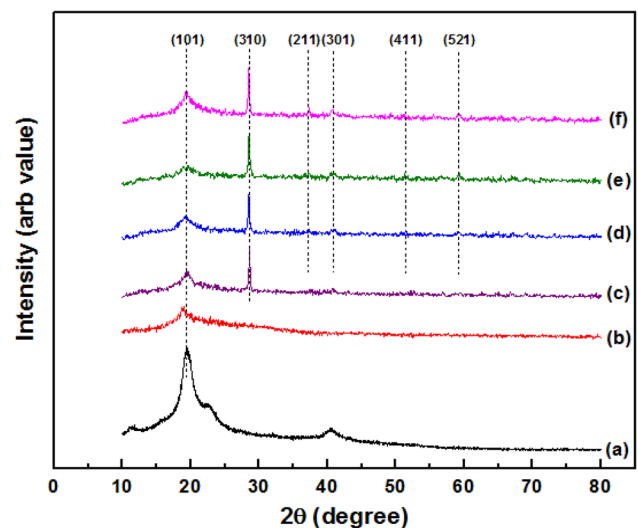$$D = K\lambda / \beta \cos\theta$$

Fig. 3 XRD Spectra of **a** pure PVA, **b** PVA/PEDOT:PSS at 50:50 wt% and PVA/PEDOT:PSS/MnO₂ at **c** 50:45:05 wt%, **d** 50:35:15 wt%, **e** 50:25:25 wt%, **f** 50:20:30 wt%

where D is the crystallite size, K is the Scherrer's constant (0.9), λ is the X-ray wavelength (1.5406 Å), β is the Full width at half maximum (calculated in radians), and θ is the diffraction angle.

The lattice strain (LS) was also calculated by,

$$LS = \beta \cos \theta / 4$$

The variation in the crystallite size of the composites can be determined based on the broadening of the diffraction peaks. The peaks get broadened for low crystallite sizes and the broadening decreases for large crystallite sizes which are examined by the calculation of full width half maximum (FWHM). Lattice strain also contributes to the broadening of the peak [54]. As the concentration of PEDOT:PSS and MnO_2 varies, the ionic radii of the elements vary which further causes the variation in the crystallite size. The change in the volume of the unit cell and lattice divergence among the phases cause tensile stress [53]. The hardness and efficiency of the material increase as the crystallite size decreases. Initially, the crystallite size decreases, and the lattice strain increases depicting good cohesion between the phases. But as the wt% of PEDOT:PSS decreases from 25 to 20 wt% and by increasing wt% of MnO_2 from 25 to 30 wt% crystallite size increases. This is due to the dispersion of more amount of MnO_2 fillers in the polymer blend which reduces the cohesion between the phases thus reducing lattice strain [53]. The crystallinity of the material increases by a decrease in the microstrain which corresponds to the increase in the peak intensity [55]. The calculated values of crystallite size and lattice strain for the PVA/PEDOT:PSS/MnO_2 composites are given in Table 2.

3.3 SEM characterization

The SEM micrographs for the as-synthesized PVA/PEDOT:PSS/MnO_2 composite films are depicted in Fig. 4. From the SEM image of the PVA/PEDOT:PSS blend, it is clear that the porous structures occurring due to the evaporation of water molecules reduce because of the complete penetration of the PEDOT:PSS into the PVA cross-linker [47]. Figure 4b, depicts the homogeneous dispersion of 15 wt% MnO_2 fillers in the PVA/PEDOT:PSS polymer blend, forming a flexible film with no agglomerations. The macro-sized porous structures in the PVA/PEDOT:PSS blend are reduced to mesoporous structures by the uniform dispersion and hydrophilicity of

MnO_2 [42]. But in Fig. 4c, 30 wt% MnO_2 fillers dispersed in PVA/PEDOT:PSS blend causes agglomeration and gives a rough surface morphology and improved flexibility for electrical conduction for 20 wt% of the conducting polymer PEDOT:PSS [51]. In addition, the calculation of effective densities [56] for all the sample compositions confirms that the porous structures of the polymer blend are decreasing with the incorporation of MnO_2 fillers leading to an increase in effective density for the composites. The calculated values are shown in Table 3. This confirms that the porous structures of the polymer blend are decreasing with the incorporation of MnO_2 fillers leading to an increase in effective density for the composites. The elemental study, the chemical composition of the composite films and the dispersion of MnO_2 in the polymer blend are determined by Energy-dispersive X-ray (EDX) analysis. The EDX spectra given in Fig. 4d confirm the excellent and uniform dispersion of MnO_2 in the PVA/PEDOT:PSS blend depicting the presence of Manganese (Mn) and oxygen(O) in the polymer blend and the values for element distributions are 84.52 and 15.48 (in wt%) and 61.40 and 38.60 (in atomic%) respectively and is given in Fig. 4e.

3.4 Thermogravimetric analysis

Figure 5 depicts the thermograph of the as-synthesized PVA/PEDOT:PSS/MnO_2 composite films in the temperature range of 27 °C (RT) to 800 °C. For pure PVA, the occurrence of three-stage thermal degradation is shown in the thermograph curve of Fig. 5a. In the initial thermal degradation stage from 27 to 150 °C, there is a weight loss of nearly 5.3% due to the evaporation of residual water molecules [57]. In the second thermal degradation stage between 230 and 400 °C, a huge weight loss of around 72% is appropriate for breaking bonded side chains of PVA [45]. In the third phase from 400 to 650 °C, there is a weight loss of nearly 13.9% as the main chains of the PVA molecule get degraded [58, 59]. Figure 5b from 27 to 130 °C depicts the evaporation of hydroxyl, CO, and water molecules of nearly 5.5% from the PVA/PEDOT:PSS blend [60]. In the second phase from 230 to 400 °C, there is a maximum weight loss of around 62% due to the splitting of bonded side chains. In the third phase from 400 to 650 °C, there is a wt loss of around 25% due to the degradation of carbon in the backbone of the polymer molecular chain [60, 61]. In

Table 2 Crystallite size and Lattice Strain for PVA/PEDOT:PSS/MnO$_2$ composite films for different compositions

Polymer Composites	FWHM (β)	Crystallite size (D) (nm)	Lattice Strain (ε) ($\times 10^{-3}$)
PVA/PEDOT:PSS/MnO$_2$ (50:45:05)	0.0040	34.8	0.99
PVA/PEDOT:PSS/MnO$_2$ (50:35:15)	0.0052	27	1.28
PVA/PEDOT:PSS/MnO$_2$ (50:25:25)	0.0051	27.8	1.24
PVA/PEDOT:PSS/MnO$_2$ (50:20:30)	0.0050	28	1.23

Fig. 5c–f from 27 to 130 °C almost similar thermal degradation is observed as of pure PVA and PVA/PEDOT:PSS blend. But from 230 to 400 °C, there is an increase in thermal stability as the wt % of MnO$_2$ is increased in the PVA/PEDOT:PSS blend. The weight loss of the PCs decreases with an increase in MnO$_2$ filler content. At around 300 °C, PVA/PEDOT:PSS/MnO$_2$ with wt % (50:45:05), (50:35:15), (50:25:25), (50:20:30) has wt % around 40, 41, 50, 41% and at 800 °C the residue wt% is around 5.2, 12.6, 15.5, 12.3% respectively which is comparatively higher than pure PVA and PVA/PEDOT:PSS blend. The higher thermal stability is the result of good interfacial interactions between the polymer blend and inorganic MnO$_2$ fillers of PC thus proving its fine compatibility.

3.5 Dielectric characterization

Figures 6 and 7, reveal the analyses of dielectric constant and loss for the as-synthesized PVA/PEDOT:PSS/MnO$_2$ under 50 Hz to 20 MHz frequency and 40 °C to 150 °C temperature ranges.The dielectric constant (ε) is dependent on frequency for the pure PVA, PVA/PEDOT:PSS blend and the PVA/PEDOT:PSS/MnO$_2$ films with different wt% have been depicted in Fig. 6a–f. The characterization is done at 40 °C to 150 °C for the reason that, at room temperature, the PC film absorbs less thermal energy which makes dipoles in the dielectric material immovable. So, they do not respond to the applied electric field. But as the temperature increases from 40 to 150 °C, the dipole molecules become free by acquiring thermal energy and polarizing themselves to the direction of the applied electric field [62]. The maximum dielectric constant value for pure PVA is 10.71 in 50 Hz at 150 °C which is very less. But when blending with the highly conductive PEDOT:PSS, the dielectric constant increases to the highest value of 225.2. For different filler loadings and decreasing the wt% of PEDOT:PSS, the dielectric constant increases

with a maximum value of 646.7, 1949, 325 and 1180 at a lower frequency (50 Hz) under 150 °C, 130 °C, 120 °C, and 140 °C, respectively, because of stronger interfacial polarization and dipole interactions. But at a higher frequency (5 kHz), the dielectric constant becomes zero for all the composites and remains zero when the frequency is further increased. At higher frequencies, the polarization does not respond due to disturbances in the dipole's orientation along the direction of an applied electric field. Thus the inverse effect of dielectric permittivity is observed in increasing frequency ranges. So, a fast decrease in dielectric constant is observed at low-frequency ranges and a slow decrease at high frequencies corresponding to Maxwell–Wagner–Sillars polarization [45]. With the increase in dispersion of MnO$_2$ wt%, the hopping conduction mechanism of the charge carriers increased gradually and reached the percolation threshold at 15 wt% of MnO$_2$, and the dielectric constant increased abruptly [45, 63]. This fluctuation occurring for 15 wt% of MnO$_2$ dispersed polymer blend is appropriate to rapid resonant electrical transitions than their relaxation mechanisms [26, 64]. The high conductivity causes a resonance effect [65]. But at 25 wt% and 20 wt% PEDOT:PSS with 25 wt%, and 30 wt% of MnO$_2$ loading, the dielectric constant values decrease explaining the agglomeration of the filler particles in the polymer blend. The agglomerations resist the charge carrier's movement and decrease the dielectric constant of the film. Moreover, the development of conductive network structure causes leakage current contributing to a decrease in dielectric constant [66]. The non-regularity in the dielectric permittivity is observed at higher concentrations of MnO$_2$ which could be due to the fluctuations and complexations in the interactions between the MnO$_2$ and PVA/PEDOT:PSS blend. The simultaneous decrease in PEDOT:PSS wt% also results in non-systematic variations in the PC interfaces [12, 62]. Moreover, a rise in thermal oscillations
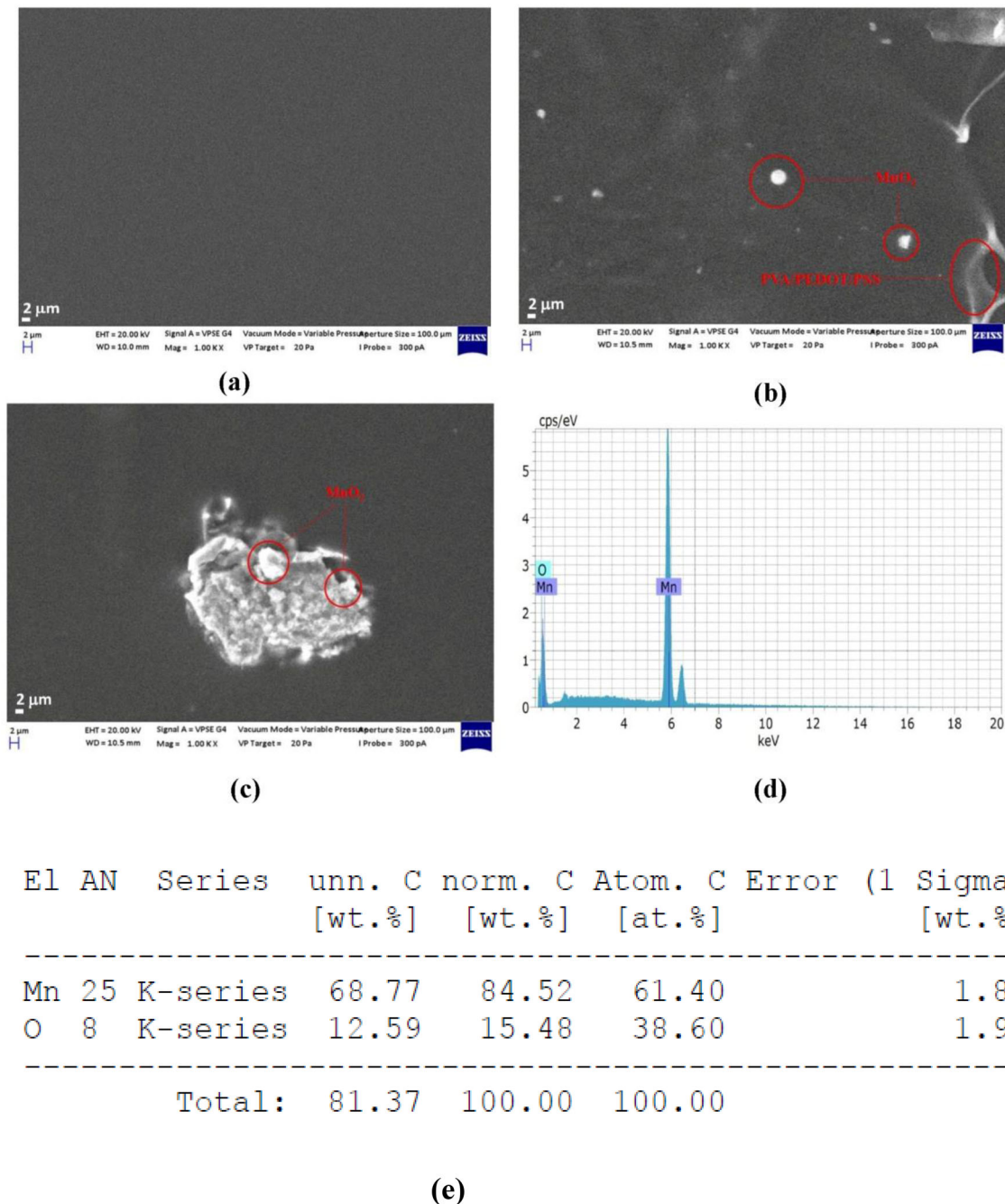
(a)

(b)

(c)

(d)

El	AN	Series	unn. C [wt.%]	norm. C [wt.%]	Atom. C [at.%]	Error (1 Sigma) [wt.%]
Mn	25	K-series	68.77	84.52	61.40	1.89
O	8	K-series	12.59	15.48	38.60	1.93
		Total:	81.37	100.00	100.00	

(e)

Fig. 4 SEM images of **a** PVA/PEDOT:PSS at 50:50 wt% and PVA/PEDOT:PSS/MnO$_2$ at **b** 50:35:15 wt%, **c** 50:20:30 wt%, **d** EDX spectrum of PVA/PEDOT:PSS/MnO$_2$ composite, **e** data of EDX analysis

at higher concentrations at higher temperatures disrupts the dipole orientation in the direction of the electric field [67]. Figure 7a–f depicts the dielectric loss (tanδ) taken for the pure PVA, PVA/PEDOT:PSS, and PVA/PEDOT:PSS/MnO$_2$ composite films. For pure PVA, the maximum dielectric loss is 1.91 at 50 Hz under 150 °C and the loss increases to 4.73 for PVA/PEDOT:PSS blend at 100 Hz under 40 °C. For

the PCs, by increasing the wt% of MnO$_2$ 5 wt%, 15 wt%, 25 wt%, 30 wt% and decreasing the wt% of PEDOT:PSS to 45 wt%, 35 wt%, 25 wt%, 20 wt% the dielectric loss has a maximum value at 9.89, 8.13, 13.06, 10.53. The accumulation of charge carriers at the sample-electrode interface causes an increase in the dielectric loss at low frequencies. The dielectric loss increases with temperature upto a certain

Table 3 Effective densities of the as-synthesized PVA/PEDOT:PSS/MnO$_2$ composites

Polymer composites	Effective density (g/cm^3)
Pure PVA	1.19
PVA/PEDOT:PSS (50:50)	1.1
PVA/PEDOT:PSS/MnO$_2$ (50:45:05)	1.3
PVA/PEDOT:PSS/MnO$_2$ (50:35:15)	1.7
PVA/PEDOT:PSS/MnO$_2$ (50:25:25)	2.1
PVA/PEDOT:PSS/MnO$_2$ (50:20:30)	2.3
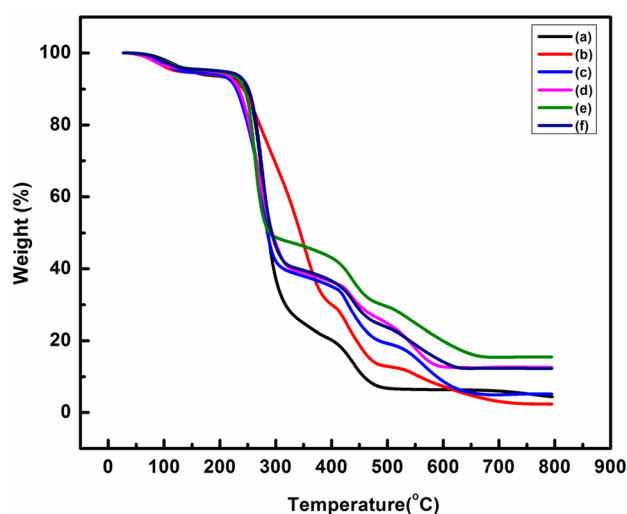
Fig. 5 TGA curves of **a** Pure PVA, **b** PVA/PEDOT:PSS blend at 50:50 wt%, **c** PVA/PEDOT:PSS/MnO$_2$ composites at 50:45:05 wt%, **d** 50:35:15 wt%, **e** 50:25:25 wt% and **f** 50:20:30 wt%

frequency for different composites due to an increase in the number of mobile ions resulting in conductivity [68]. By increasing the frequency to 1 MHz, the dielectric loss becomes almost zero and remains zero with a further increase in frequency. It is observed that the dielectric loss decreases from 13.06 to 10.53 due to agglomeration resulting in a decrease in segment mobility of the composite [64]. Thus, the as-synthesized PC films correspond to an excellent interfacial interaction between MnO$_2$ and PVA/PEDOT:PSS blend.As the synthesised films possess high dielectric constant and low dielectric loss values, the resultant electrical properties nominate [69] these materials to be an excellent choice in small-scale integrated circuits. The observed values of dielectric constant and loss are reported in Table 4. Table 5 depicts the comparison of the present work on PVA/PEDOT:PSS/MnO$_2$ with the literature on other polymer composites [66, 67, 70–75]. However, in the

case of ceramics dispersed polymer composites, when examined at high temperatures and at radio frequencies, the obtained values of dielectric constant and loss are found to be low and the electrical resistivity is very high [55, 76–79].

3.5.1 Quality factor

Figure 8a–e depicts the Q-factor of the PVA/PEDOT:PSS/MnO$_2$ composite films. Q-factor has a significant role in the analysis of LC or resonant tank circuits [80]. Q-factor is a function of frequency and temperature and it is a dimensionless quantity. By this analysis, the ratio of energy or electric charges stored to the energy loss in a system (inductor or capacitor) at a particular frequency and temperature can be determined [81]. In simple words, the efficiency of the reactive system can be calculated. The temperature plays an important role in contributing to the rate of loss of energy per unit cycle which is called dielectric relaxation [20].

$$Q = \frac{2\pi \, (\text{Maximum instantaneous energy stored})}{\text{The energy dissipated per cycle}}$$

It is well observed that Q-factor is very low in the low-frequency range (< 5 kHz), minimum in the intermediate frequency range (5 kHz-1 MHz), and attains a maximum value at the high frequency (10 MHz). The Q-factor for PVA/PEDOT:PSS blend attains a maximum value of 81.8 at 10 MHz at 100 °C. At 45 wt% PEDOT:PSS and 5 wt% MnO$_2$ loading, the Q-factor attains a maximum value of 13.1 at 10 MHz. At 35 wt% PEDOT:PSS and 15 wt% MnO$_2$ loading, the Q-factor possesses a maximum value of 10.3 at 10 MHz. This shows that the increase in the MnO$_2$ wt% loading in the PVA/PEDOT:PSS blend decreases the Q-factor of the PC films. The increase in the conductivity of the films indicates that the conductivity and Q-factor are inversely proportional to one another [82]. Also, by 25 wt% PEDOT:PSS and 25 wt% MnO$_2$ loading, there is a slight increase in the Q-factor to 25.6 from 10.3 at 10 MHz. Thus, by this analysis, it is concluded that the as-synthesized PC films can be the best option for electronic device fabrications. The observed Q-factor values for the as-synthesized PC films are shown in Table 6. In the literature, PEDOT:PSS/DMSO nanocomposite films [83] report a Q- factor value of 6.0 × 10^{-4} for 5 wt% of DMSO doped in PEDOT:PSS. Few authors have
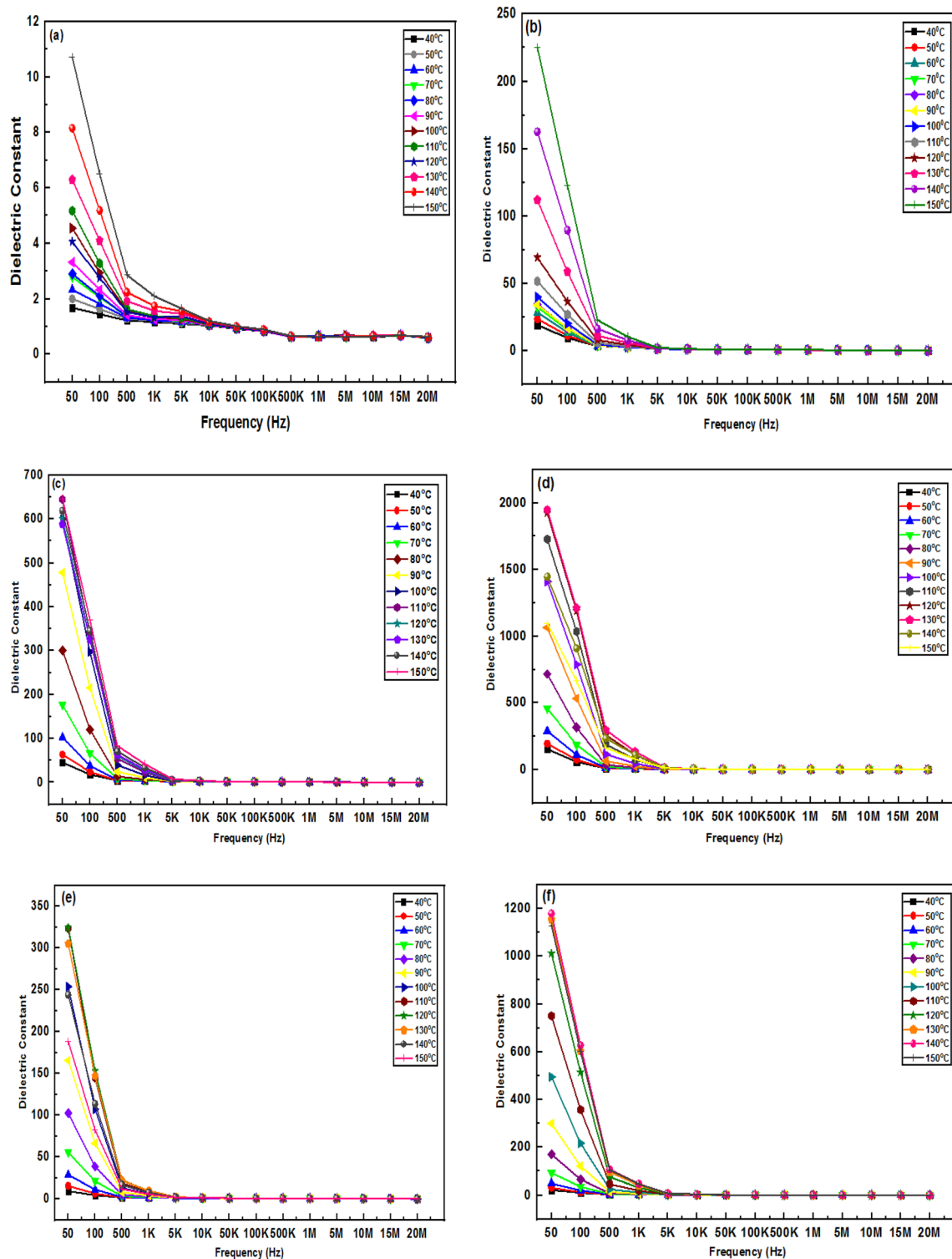
Fig. 6 Dielectric constant (ε) of **a** Pure PVA, **b** PVA/PEDOT:PSS at 50:50 wt% and PVA/PEDOT:PSS/MnO$_2$ composites at **c** 50:45:05 wt%, **d** 50:35:15 wt%, **e** 50:25:25 wt%, **f** 50:20:30 wt%
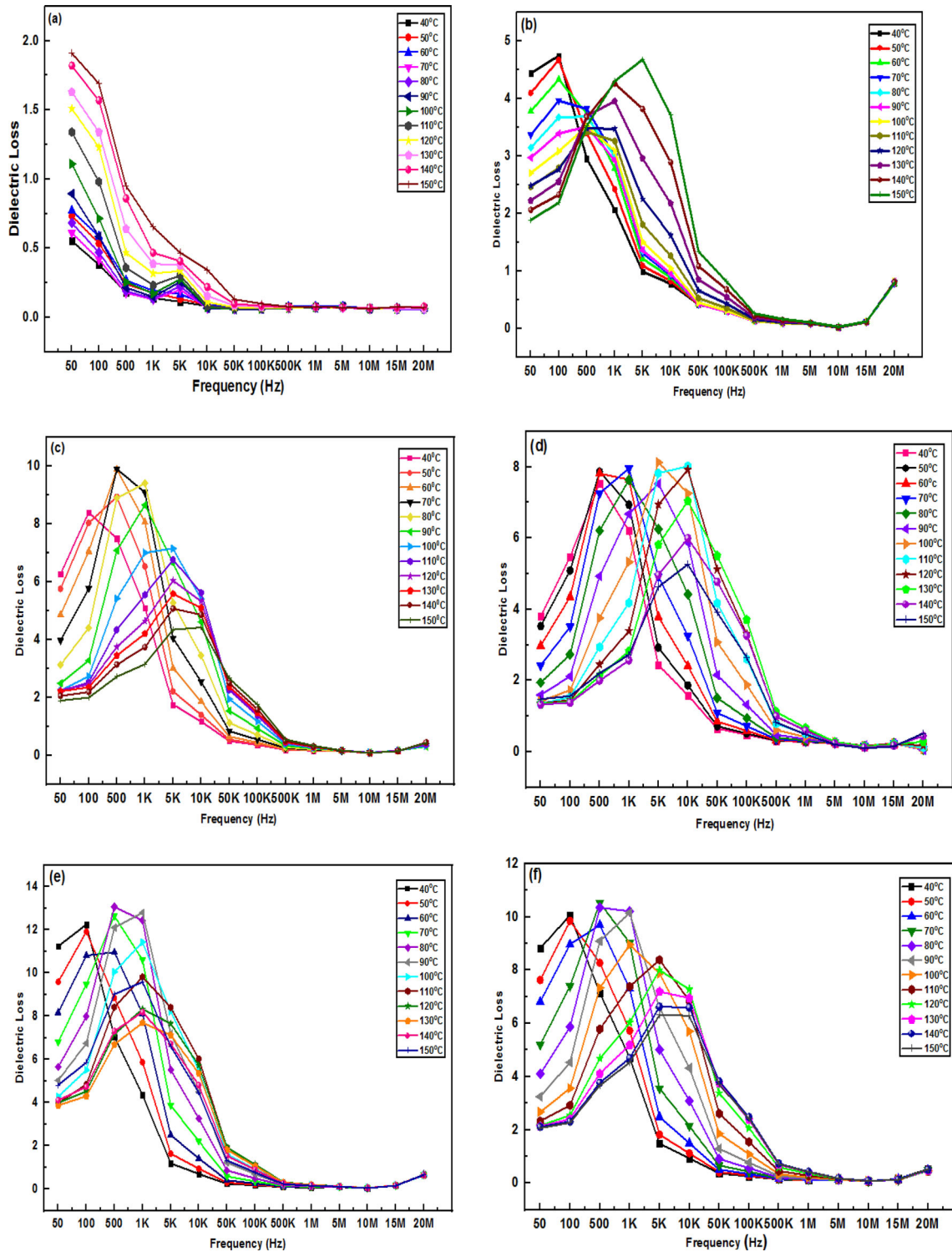
Fig. 7 Dielectric loss (tanδ) of **a** Pure PVA, **b** PVA/PEDOT:PSS at 50:50 wt% and PVA/PEDOT:PSS/MnO$_2$ composites at **c** 50:45:05 wt%, **d** 50:35:15 wt%, **e** 50:25:25 wt%, **f** 50:20:30 wt%

Table 4 Maximum value of dielectric constant and loss of PVA/PEDOT:PSS/MnO$_2$ composite films for different compositions

Polymer composites	Dielectric constant (ε)	Dielectric loss (tanδ)
Pure PVA	10.71 at 50 Hz, 150 °C	1.91 at 50 Hz, 150 °C
PVA/PEDOT:PSS (50:50)	225.2 at 50 Hz, 150 °C	4.73 at 100 Hz, 40 °C
PVA/PEDOT:PSS/MnO$_2$ (50:45:05)	646.7 at 50 Hz, 150 °C	9.89 at 500 Hz, 70 °C
PVA/PEDOT:PSS/MnO$_2$ (50:35:15)	1949 at 50 Hz, 130 °C	8.13 at 5 kHz, 100 °C
PVA/PEDOT:PSS/MnO$_2$ (50:25:25)	325 at 50 Hz, 120 °C	13.06 at 500 Hz, 80 °C
PVA/PEDOT:PSS/MnO$_2$ (50:20:30)	1180 at 50 Hz, 140 °C	10.53 at 500 Hz, 70 °C

Table 5 Comparison of dielectric constant and dielectric loss of other polymer composite films

Polymer composites	Frequency (Hz)	Dielectric constant (ε)	Dielectric loss (tanδ)	References
PVA/TiO$_2$	1 kHz	24.6	0.1–1.0	[70]
PVA/PVP/SnO	1 MHz	12.118	1.005	[71]
PVA/PEDOT:PSS	1 kHz	1279	0–10	[67]
rGO-MnO$_2$-PANA/PVA	10 kHz	45.0721	0.8743	[72]
BaTiO$_3$/PBT	2.45-5 GHz	21	0.015–0.023	[73]
NR-βMnO$_2$-PVDF	100 Hz	862	2.8	[66]
Bulk MnO$_2$-PVDF	$10^2 - 10^6$ Hz	12.8	Below 0.15	[66]
CNT/MnO$_2$NWs/PVDF	8.2–12.4 GHz	50.6	0.7	[74]
PVA/PEO/MnO$_2$	100 Hz	$\sim$ 3.9	$\sim$ 5.8	[75]
PVA/PEDOT:PSS/MnO$_2$ wt% 50:35:15	50 Hz, 5 kHz	1949	8.13	Present work

already reported, a negative Q-factor value. For example; Joshi et al.depicted that for PVA doped NiCl$_2$ composite films at 1 MHz, the Q-factor showed a negative value which is due to the damping of electric charges [84].

4 Conclusions

In this work, PVA/PEDOT:PSS/MnO$_2$ composite films at different concentrations have been fabricated by the solution casting method, and its various characterization techniques have been investigated using different analysis techniques. FTIR results inferred a good interaction between PVA/PEDOT:PSS and MnO$_2$ and a good dispersion of MnO$_2$ in the polymer matrix. The crystallinity of the polymer composite was observed by XRD technique and the crystallite size varied with an increase in the incorporation of MnO$_2$ fillers. The SEM images depicted an excellent and uniform dispersion at low concentrations and agglomeration at high concentrations of MnO$_2$ fillers in PVA/PEDOT:PSS and the elemental distribution was examined through EDX spectra. TGA results indicated that the thermal stability increases by the addition of MnO$_2$ fillers in the PVA/PEDOT:PSS blend. The dielectric results reveal that PVA/PEDOT:PSS/MnO$_2$ composite films with wt% 50:35:15 experienced the high dielectric constant 1949 with a dielectric loss of 8.13. At higher concentrations of MnO$_2$, the dielectric constant decreased due to leakage current. From the Q-factor results, it is established that the Q-factor value decreases with an increase in MnO$_2$ incorporation. Among the synthesized PC films, PVA/PEDOT:PSS/MnO$_2$ (50:35:15) showed the Q-factor value of 10.3 at 10 MHz which exhibits the excellent conductivity of the PC film. Since the synthesized PC films demonstrate superior dielectric behaviour, excellent conductivity, and better thermal stability they can be effectively used in gas and humidity sensing applications, field effect transistors, small-scale integrated circuits, actuators, and flexible capacitors.
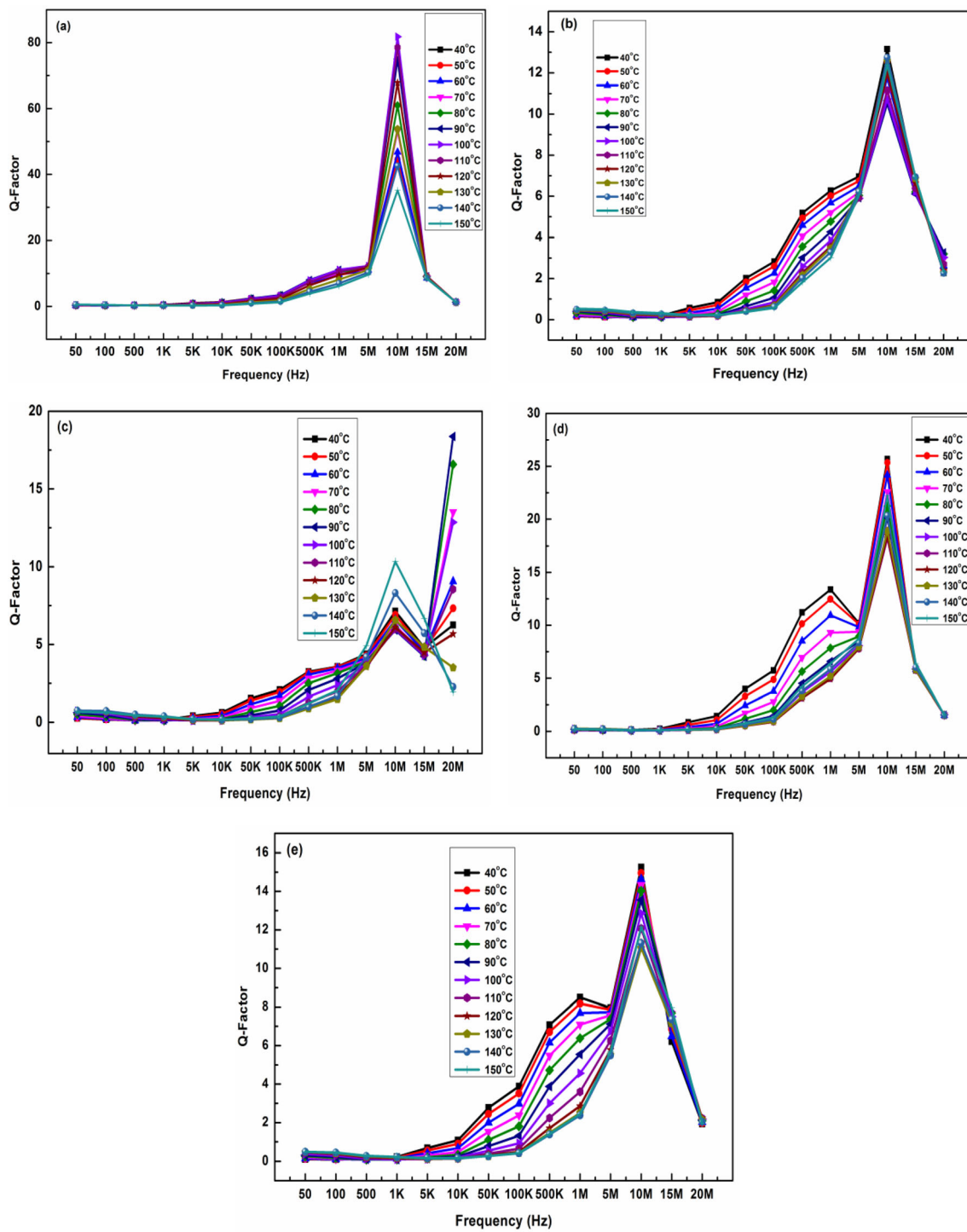
Fig. 8 Quality factor of **a** PVA/PEDOT:PSS at 50:50 wt% and PVA/PEDOT:PSS/MnO$_2$ composite films at **b** 50:45:05 wt%, **c** 50:35:15 wt%, **d** 50:25:25 wt%, **e** 50:20:30 wt%

Table 6 Maximum quality factor values for PVA/PEDOT:PSS/MnO_2 composite films for different feed compositions

Polymer composites	Q-factor
PVA/PEDOT:PSS (50:50)	81.8 at 10 MHz, 100 °C
PVA/PEDOT:PSS/MnO_2 (50:45:05)	13.1 at 10 MHz, 40 °C
PVA/PEDOT:PSS/MnO_2 (50:35:15)	10.3 at 10 MHz, 150 °C
PVA/PEDOT:PSS/MnO_2 (50:25:25)	25.6 at 10 MHz, 40 °C
PVA/PEDOT:PSS/MnO_2 (50:20:30)	15.2 at 10 MHz, 40 °C

Author contributions

The corresponding author confirms that the authors mentioned in this paper have equally contributed to bringing out this work and also in the preparation of this manuscript.

Data availability

The data used in the manuscript shall be made available on request.

Declarations

References

1. J.G. Mallete, A. Márquez, O. Manero, R. Castro-Rodrigues, Pol. Eng. Sci. **40**, 2272–2278 (2000)
2. D.I. Tishkevich, S. Grabchikov, S. Lastovskii, S. Trukhanov, T. Zubar, D. Vasin, A.V. Trukhanov, ACS Appl. Energy Mater. **1**, 1695–1702 (2018)
3. D.I. Tishkevich, S.S. Gracchikov, L.S. Tsybulskaya, V.S. Shendyukov, S.S. Perevoznikov, S.V. Trukhanov, E.L. Trukhanov, J. Alloys Compd. **735**, 1943–1948 (2018)
4. D.I. Tishkevich, A.I. Vorobjova, D. Vinnik, Solid State Phenom. **299**, 100–106 (2020)
5. Y. Slimani, N.A. Algarou, M.A. Almessiere, A. Sadaqat, M.G. Vakhitov, D.S. Klygach, D.I. Tishkevich, A.V. Trukhanov, S. Guner, A.S. Hakeem, I.A. Auwal, A. Baykal, A. Manikandan, I. Ercan, Arab. J. Chem. **14**, 102992 (2021)
6. A.V. Trukhanov, D.I. Tishkevich, S.V. Podgornaya, E. Kaniukov, M.A. Darwish, T.I. Zubar, A.V. Timofeev, E.L. Trukhanova, V.G. Koshishin, S.V. Trukhanov, Nanomaterials **12**, 868 (2022)
7. E.M. ShehaMona, M. NasrMabrouk, K.E. Mansy, J. Adv. Res. **6**, 563–569 (2015)
8. A. Bouzidi, W. Jilani, I.S. Yahia, H.Y. Zahran, M.A. Assiri, J. Inorg. Organomet. Poly Mat. **30**, 3940–3952 (2020)
9. R. Ambrosio, A. Carrillo, M.L. Mota, K. Torre, R. Torrealba, M. Moreno, H. Vazquez, J. Flores, I. Vivaldo, Polymer **10**, 1370 (2018)
10. F.E. Sayed, M.I. Mohammed, I.S. Yahia, J. Mater. Sci. **31**, 10408–10421 (2020)
11. S. Mallakpour, M. Lormahdiabadi, J. Polym. Res. **27**, 259 (2020)
12. P. Rani, M.B. Ahamed, K. Deshmukh, J. Appl. Polym. Sci. **137**, 49392 (2020)
13. H.N. Fard, G.B. Pour, M.N. Sarvi, P. Esmaili, Ionics **25**, 2951–2963 (2019)
14. K. Deshmukh, M.B. Ahamed, R.R. Deshmukh, S.K.K. Pasha, K.K. Sadasivuni, D. Ponnamma, K. Chidambaram, Euro Polym. J. **76**, 14–27 (2016)
15. K. Deshmukh, M.B. Ahamed, K.K. Sadasivuni, D. Ponnamma, M.A.A. AlMaadeed, S.K.K. Pasha, R.R. Deshmukh, K. Chidambaram, Mater. Chem. Phys. **186**, 188–201 (2017)
16. K. Deshmukh, M.B. Ahamed, A.R. Polu, K.K. Sadasivuni, S.K.K. Pasha, D. Ponnamma, M.A.A. Al-Maadeed, R.R. Deshmukh, K. Chidambaram, J. Mater. Sci. **27**, 11410–11424 (2016)
17. T. Zhang, K. Li, C. Li, S. Ma, H.H. Hng, L. Wei, Adv. Elect. Mater. **3**, 1600554 (2017)
18. A. Yamasaki, T. Shinbo, K. Mizoguchi, J. Appl. Poly. **64**, 1061–1065 (1997)
19. B. Karthikeyan, Physica B **364**, 328–332 (2005)
20. K. Deshmukh, S. Sankaran, M.B. Ahamed, S.K.K. Pasha, K.K. Sadasivuni, D. Ponnamma, M.A.A. AlMaadeed, K. Chidambaram, Int. J. Nanosci. **16**, 1760005 (2017)
21. F. Hamidouche, M.M.S. Sanad, Z. Ghebache, N. Boudieb, J. Mol. Struct. **1251**, 131964 (2022)
22. F. Hamidouche, Z. Ghebache, N. Boudieb, M. Sanad, N.E. Djelali, J. Inorg. Organometall. Polym. Mater. **31**, 704–715 (2021)
23. C.I. Idumah, Syn. Met. **273**, 116674 (2021)
24. J.H. Oh, G.W. George, A.D. Martinez, L.C. Moores, M.J. Green, Polymer **230**, 124077 (2021)
25. P. Li, K. Sun, J. Ouyang, ACS Appl. Mater. Interfaces **7**, 18415–18423 (2015)
26. C. Chen, A. Kine, R.D. Nelson, J.C. LaRue, Synth. Met. **206**, 106–114 (2015)
27. B. Baruah, A. Kumar, Synth. Met **245**, 74–86 (2018)
28. W. Yao, L. Li, Z. Bai, Y. Jiang, L. Xu, J. Yan, Y. Wan, R. Tan, H. Liu, P. Liu, Int. J. Electrochem. Sci. **15**, 9135–9145 (2020)

29. S. Park, C.W. Lee, J.M. Kim, Org. Electron. **58**, 1–5 (2018)

30. J. Ouyang, Smart Mater. **2**, 263–281 (2021)

31. O. Carr, G. Gozzi, L.F. Santos, R.M. Faria, D.L. Chinaglia, Transl. Mater. Res. **2**, 015002 (2015)

32. Y. Wang, Y. Ding, X. Guo, G. Yu, Nano Res **12**, 1978–1987 (2019)

33. M. Moharam, M.M.S. Sanad, E.M.E. Sayed, M.E. Ibrahim, IOP Conf. Ser. Mater. Sci. Eng. **762**, 012002 (2020)

34. Y. Wang, Y.Z. Zhang, Y.Q. Gao, G. Sheng, J.E. Elshof, Nano Energy **68**, 104306 (2020)

35. H.E. Wang, D. Qian, Mater. Chem. Phys. **109**, 399–403 (2008)

36. M. Sanad, A. Toghan, Appl. Phys. **127**, 1–15 (2021)

37. K. Dai, L. Lu, C. Liang, J. Dai, Q. Liu, Y. Zhang, G. Zhu, Z. Liu, Electrochim Acta **116**, 111–117 (2014)

38. M. Jayashree, M. Parthibavarman, R. Boopathiraja, S. Prabhu, R. Ramesh, J. Mater. Sci. **31**, 6910–6918 (2020)

39. M.M.S. Sanad, A.K. Yousef, M.M. Rashad, A.H. Naggar, A.Y.E. Sayed, Physica B **579**, 411889 (2020)

40. S. Pradhan, D. Goswami, D. Ganguly, S.K. Ghorai, D. Ratna, S. Chattopadhyay, Polym. Test **90**, 106716 (2020)

41. R. Yuksel, H.E. Unalan, Int. J. Energy Res. **39**, 2042–2052 (2015)

42. R. Ranjusha, K.M. Sajesh, S. Roshny, V. Lakshmi, P. Anjali, T.S. Sonia, A.S. Nair, K.R.V. Subramanian, S.V. Nair, K.P. Chennazhi, A. Balakrishnan, Microporous Mesoporous Mater. **186**, 30–36 (2014)

43. M.K. Mohanapriya, K. Deshmukh, M.B. Ahamed, K. Chidambaram, S.K.K. Pasha, Mater. Today **3**, 1864–1873 (2016)

44. M.K. Mohanapriya, K. Deshmukh, K. Chidambaram, M.B. Ahamed, K.K. Sadasivuni, D. Ponnamma, M.A.A. AlMaadeed, R.R. Deshmukh, S.K. Khadheer Pasha, J. Mater. Sci. **28**, 6099–6111 (2017)

45. P. Rani, M.B. Ahamed, K. Deshmukh, J. Mater. Sci. **32**, 764–779 (2021)

46. K. Deshmukh, M.B. Ahamed, K.K. Sadasivuni, D. Ponnamma, R.R. Deshmukh, S.K.K. Pasha, M.A.A. AlMaadeed, K. Chidambaram, J. Polym. Res. **23**, 159 (2016)

47. Y.F. Zhang, M.M. Guo, Y. Zhang, C.Y. Tang, C. Jiang, Y. Dong, W.C. Law, F.P. Du, Polym. Test **81**, 106213 (2020)

48. J. Yu, W. Gu, H. Zhao, G. Ji, Sci. China Mater. **64**, 1723–1732 (2021)

49. S. Palsaniya, H.B. Nemade, A.K. Dasmahapatra, Carbon **150**, 179–190 (2019)

50. S. Mallakpour, F. Motirasoul, Ultrasonography **40**, 410–418 (2018)

51. X. Li, C. Zhou, L. Shen, W. Zhou, J. Xu, C. Luo, J. Hou, R. Tan, F. Jiang, Int. J. Electrochem. Sci. **14**, 4632–4642 (2019)

52. Y. Chen, J. Xu, Y. Yang, Y. Zhao, W. Yang, X. Mao, M. Xin, S. Li, Electrochim Acta **193**, 199–205 (2016)

53. P. Komalavalli, I. B. S. Banu, M. H. Mamat, M. S. Anwar, S. Hussain, S. S. Basha, R. Rajesh, 2022, **5**, 529–536

54. A. Monshi, M.R. Foroughi, M.R. Monshi, World J. Nano Sci. Eng. **2**, 154–160 (2012)

55. M.M.S. Sanad, M.M. Rashad, E.A.A. Aal, M.F.E. Shahat, Ceram. Int. **39**, 1547–1554 (2013)

56. D.I. Tishkevich, T.I. Zubar, A.L. Zhaludkevich, I.U. Razanau, T.N. Vershinina, A.A. Bondaruk, E.K. Zheleznova, M. Dong, M.Y. Hanfi, M.I. Sayyed, M.V. Silibin, S.V. Trukhanov, A.V. Trukhanov, Nanomaterials **12**, 1642 (2022)

57. G. Ma, D. Yang, D. Su, X. Mu, J.F. Kennedy, J. Nie, Polym. Adv. Technol. **21**, 189–195 (2010)

58. K. Deshmukh, M.B. Ahamed, R.R. Deshmukh, P.R. Bhagat, S.K.K. Pasha, A. Bhagat, R. Shirbhate, F. Telare, C. Lakhani, Polym. Plas Techol. Eng. **55**, 231–241 (2016)

59. S.J. Lue, J.Y. Chen, J.M. Yeng, J. Macromol. Sci. B **47**, 39–51 (2007)

60. V. Hebbar, R.F. Bhajantri, H.B. Ravikumar, S. Ningaraju, J. Phys. Chem. Solids **126**, 242–256 (2019)

61. H. Du, Z. Song, J. Wang, Z. Liang, Y. Shen, F. You, Sens. Actuators A **228**, 1–8 (2015)

62. D.A. Nasrallah, M.A. Ibrahim, J. Polym. Res. **29**, 1–20 (2022)

63. D. Singh, N.L. Singh, P. Kulriya, A. Tripathi, D.M. Phase, J. Compos. Mater. **44**, 3165–3178 (2010)

64. T. Anjitha, T. Anilkumar, G. Mathew, M.T. Ramesan, Polym. Compos. **40**, 2802–2811 (2019)

65. A. Gupta, V. Choudhary, Compos. Sci. Technol. **71**, 1563–1568 (2011)

66. G.S. Wang, L.Z. Nie, S.H. Yu, RSC Adv. **2**, 6216–6221 (2012)

67. V. Mydhili, S. Manivannan, Polym. Bull. **76**, 4735–4752 (2019)

68. S. More, R. Dhokne, S. Moharil, Polym. Bull. **75**, 909–923 (2018)

69. A.S. Roy, S. Gupta, S. Sindhu, A. Parveen, P.C. Ramamurthy, Composites B **47**, 314–319 (2013)

70. S. Sugumaran, C.S. Bellan, Optik **125**, 5128–5133 (2014)

71. V. Siva, D. Vanitha, A. Murugan, A. Shameem, S.A. Bahadur, Compos. Commun. **23**, 100567 (2021)

72. A.H. Majeed, E.T.B.A. Tikrity, D.H. Hussain, Polym. Polym. Compos. **29**, 1089–1100 (2021)

73. S.B. Basturk, C.E.J. Dancer, T. McNally, J. Appl. Polym. Sci. **138**, 50521 (2021)

74. A.S. Zeraati, S.A. Mirkhani, U. Sundararaj, J. Phys. Chem. **121**, 8327–8334 (2017)

75. A. Hashim, M.A. Habeeb, Q.M. Jebur, Egypt J. Chem. **62**, 735–749 (2019)

76. M. Vikulova, A. Tsyganov, A. Bainyashev, D. Artyukhov, A. Gorokhovsky, D. Muratov, N. Gorshkov, J. Appl. Polym. Sci. **138**, 51168 (2021)

77. M.M.S. Sanad, M.M. Rashad, E.A.A. Aal, K. Powers, Mater. Chem. Phys. **162**, 299–307 (2015)

78. M.M.S. Sanad, M.M. Rashad, E.A.A. Aal, M.F.E. Shahat, J Euro Ceram. Soc. **32**, 4249–4255 (2012)

79. M.M.S. Sanad, M.M. Rashad, E.A.A. Aal, M.F.E. Shahat, K. Powers, J. Mater. Sci. **25**, 2487–2493 (2014)

80. K.D. Satapathy, K. Deshmukh, M.B. Ahamed, K.K. Sadasivuni, D. Ponnamma, S.K.K. Pasha, M.A.A. Al-Maadeed, J. Ahmed, Adv. Mater. Lett. **8**(3), 288–294 (2017)

81. K. Deshmukh, M.B. Ahamed, S. Sankaran, S.K.K. Pasha, K.K. Sadasivuni, D. Ponnamma, M.A.A. Al-Maadeed, Mater. Today **5**, 8744–8752 (2018)

82. M.K. Mohanapriya, K. Deshmukh, K.K. Sadasivuni, G. Thangamani, K. Chidambaram, M.B. Ahamed, S.K.K. Pasha, Mater. Today **9**, 199–216 (2019)

83. A. Pasha, A.S. Roy, M.V. Murugendrappa, O.A.A. Hartomy, S. Khasim, J. Mater. Sci. **27**, 8332–8339 (2016)

84. G.M. Joshi, M.T. Cuberes, Ionics **19**, 947–950 (2013)